Arc-shaped structure factor in the J_1-J_2-J_3 classical Heisenberg model on the triangular lattice

Cecilie Glittum and Olav F. Syljuåsen

Department of Physics, University of Oslo, P.O. Box 1048 Blindern, N-0316 Oslo, Norway

We study the J_1-J_2-J_3 classical Heisenberg model with ferromagnetic J_1 on the triangular lattice using the nematic bond theory. For parameters where the momentum space coupling function $J_{\vec{q}}$ shows a discrete set of minima, we find that the system in general exhibits a single first-order phase transition between the high-temperature ring liquid and the low-temperature single-$\vec{q}$ planar spiral state. Close to where $J_{\vec{q}}$ shows a continuous minimum, we on the other hand find several phase transitions upon lowering the temperature. Most interestingly, we find an intermediate temperature "arc" regime, where the structure factor breaks rotational symmetry and shows a broad arc-shaped maximum. We map out the parameter region over which this arc regime exists and characterize details of its static structure factor over the same region.

I. INTRODUCTION

The Mermin-Wagner theorem [1] forbids magnetic long-range order in two-dimensional Heisenberg magnets at finite temperatures. Nevertheless, such magnets may still exhibit phase transitions where a *discrete* point group symmetry of the lattice is broken. The type of order to expect in such cases is usually that of a single-$\vec{q}$ planar spiral state with a pitch vector taken from the set of wave vectors $\vec{Q}$ that minimize the coupling function in momentum space $J_{\vec{q}}$. Lattice point group symmetries will transfer the $\vec{Q}$s into one another and can be broken if the different $\vec{Q}$s correspond to inequivalent spin states under global continuous spin rotations [2].

This scenario becomes more complicated when the $\vec{Q}$s form a continuous set. In those cases the entropy, in contrast to the energy $J_{\vec{q}}$, may favor a discrete subset of the $\vec{Q}$s and so there can still be phase transitions breaking lattice point group symmetries at finite temperatures. This *order by disorder* scenario [3–5] happens in particular for the Heisenberg antiferromagnet on the honeycomb lattice for sufficiently large second neighbor coupling [6,7] and on the square lattice when a third neighbor coupling is included [8]. In all these cases, the order to expect can be inferred by finding the $\vec{Q}$s corresponding to maximal spin wave entropy.

Here we investigate the lattice symmetry breaking phase transitions of the classical Heisenberg model on the triangular lattice. Spontaneous breaking of lattice symmetries does not happen for the nearest neighbor model. Therefore, we add second and third neighbor interactions as shown in Fig. 1. The Hamiltonian is

$$H = J_1 \sum_{\langle i,j \rangle} \vec{S}_i \cdot \vec{S}_j + J_2 \sum_{\langle\langle i,j \rangle\rangle} \vec{S}_i \cdot \vec{S}_j + J_3 \sum_{\langle\langle\langle i,j \rangle\rangle\rangle} \vec{S}_i \cdot \vec{S}_j. \quad (1)$$

This J_1-J_2-J_3 Heisenberg model has several distinct phases at zero temperature [9]. At finite temperatures in a magnetic field it is known to have a skyrmion lattice phase [10]. It has been proposed as a model for $NiGa_2S_4$ [11–13], and its

spin-1/2 version has been studied in the context of quantum spin liquids [14,15]. The extended couplings allow us to tune $J_{\vec{q}}$ between discrete and continuous minima. For this J_1-J_2-J_3 Heisenberg model with ferromagnetic J_1, we also find the order by disorder scenario, but it plays out in an interesting way. Our main result is that the ordering occurs via a sequence of *two* phase transitions as the temperature is lowered. Particularly interesting is the intermediate phase, where the static structure factor is dominated by an arc-shaped ridge. This arc breaks lattice rotational symmetry, but not all mirror symmetries, and is not a single-$\vec{q}$ state.

To be able to efficiently investigate large portions of parameter space, we employ the nematic bond theory (NBT) [16], which is a set of approximate self-consistent equations for classical Heisenberg magnets. The equations can be solved numerically for large lattices [17]. Besides calculating order parameters and correlation functions, we show here that the NBT can also be used to calculate the free energy directly, which allows us to determine the order of the phase transitions. We explain the NBT with an emphasis on how to obtain the free energy in Sec. II. The details of the J_1-J_2-J_3 model on
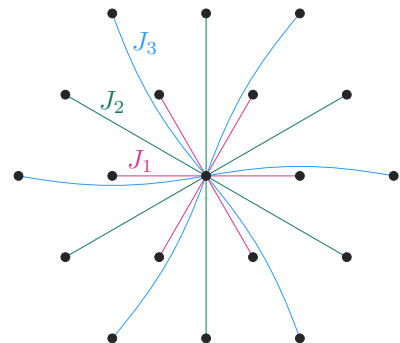

FIG. 1. The triangular lattice with up to third nearest neighbor interactions.

the triangular lattice are given in Sec. III, and the results are presented in Sec. IV. We end with a discussion in Sec. V.

II. METHOD

The NBT is conveniently formulated in momentum space:

$$H = \sum_{\vec{q}} J_{\vec{q}} \vec{S}_{-\vec{q}} \cdot \vec{S}_{\vec{q}}, \tag{2}$$

where the sum goes over the first Brillouin zone. The classical spins on all sites are unit length vectors: $|\vec{S}_{\vec{r}}| = 1$. These length constraints are enforced in the partition function as integral representations of δ functions

$$\delta\big(|\vec{S}_{\vec{r}}| - 1\big) = \int_{-\infty}^{\infty} \frac{\beta d\lambda_{\vec{r}}}{\pi} \, e^{-i\beta\lambda_{\vec{r}}(\vec{S}_{\vec{r}}\cdot\vec{S}_{\vec{r}} - 1)}, \tag{3}$$

where we have scaled the integration variable $\lambda_{\vec{r}}$ by the inverse temperature, $\beta = 1/T$. This gives the partition function

$$Z = \int D\vec{S} \, d\Delta \, D\lambda \, e^{-\beta \sum_{\vec{q},\vec{q}'} (\mathbf{K}_{\vec{q},\vec{q}'} - \mathbf{\Lambda}_{\vec{q},\vec{q}'}) \vec{S}_{\vec{q}}^{*} \cdot \vec{S}_{\vec{q}'} + \beta V \Delta}, \tag{4}$$

where we have introduced a momentum space matrix $\mathbf{\Lambda}_{\vec{q},\vec{q}'} \equiv -i\lambda_{\vec{q}-\vec{q}'}(1 - \delta_{\vec{q},\vec{q}'})$, and $\lambda_{\vec{q}}$ is the Fourier-transformed constraint integration variable. We have separated out its $\vec{q} = 0$ component and written it as $\Delta \equiv i\lambda_{\vec{q}=0}$ and put it into another momentum space matrix $\mathbf{K}_{\vec{q},\vec{q}'} \equiv K_{\vec{q}} \, \delta_{\vec{q},\vec{q}'}$, where $K_{\vec{q}} \equiv J_{\vec{q}} + \Delta$. The integration measures are always redefined to include factors of volume V, β, π, and $-i$. The inverse of $K_{\vec{q}}$ is essentially the spin-spin correlation function in momentum space, and Δ can be interpreted as the average constraint, similar to the self-consistent field in the self-consistent Gaussian approximation. The NBT goes beyond this as it also accounts for the fluctuations $\mathbf{\Lambda}_{\vec{q},\vec{q}'}$ around the average constraint. This is essential in order to capture lattice point group symmetry breaking phase transitions.

The integrals over the spin components can now be taken as independent Gaussian integrals. We generalize the spins to have N_s vector components but will set $N_s = 3$ at the end of the calculation. We scale the spin components by a factor $1/\sqrt{\beta}$ and perform the Gaussian integrals to get

$$Z = \int d\Delta \, D\lambda \, e^{-S[\Delta,\lambda]}, \tag{5}$$

where the effective constraint action is

$$S[\Delta, \lambda] \equiv \frac{N_s}{2} \text{Tr} \ln (\mathbf{K} - \mathbf{\Lambda}) - \beta V \Delta. \tag{6}$$

Expanding this expression in powers of $\mathbf{\Lambda}$, we get

$$S[\Delta, \lambda] = -\beta V \Delta + \frac{N_s}{2} \text{Tr} \ln \mathbf{K} + \frac{1}{2} \sum_{\vec{q} \neq 0} \lambda_{-\vec{q}} D_{0,\vec{q}}^{-1} \lambda_{\vec{q}} + S_r, \tag{7}$$

where we have used the quadratic term in $\mathbf{\Lambda}$ to give the inverse constraint propagator $\mathbf{D_0^{-1}}_{\vec{q}\vec{q}'} \equiv D_{0,\vec{q}}^{-1} \delta_{\vec{q},\vec{q}'}$ with

$$D_{0,\vec{q}}^{-1} = \frac{N_s}{2} \sum_{\vec{p}} K_{\vec{p}+\vec{q}}^{-1} K_{\vec{p}}^{-1}, \tag{8}$$
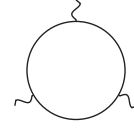

FIG. 2. A ring with three wavy hooks; the $n = 3$ term in S_r.

and the interaction S_r is

$$S_r = -\frac{N_s}{2} \sum_{n=3}^{\infty} \frac{1}{n} \text{Tr}(\mathbf{K}^{-1}\mathbf{\Lambda})^n. \tag{9}$$

There is no linear term in $\mathbf{\Lambda}$ because $\mathbf{\Lambda}$ has no diagonal components, which follows from separating out $\lambda_{\vec{q}=0}$.

We then treat S_r as a perturbation about the Gaussian action defined by the quadratic terms in λ and integrate over λ so that

$$Z = \int d\Delta \, e^{-S[\Delta]}, \tag{10}$$

where

$$S[\Delta] \equiv -\beta V \Delta + \frac{N_s}{2} \text{Tr} \ln \mathbf{K} + \frac{1}{2} \text{Tr} \ln \mathbf{D_0^{-1}} - \ln \langle e^{-S_r} \rangle. \tag{11}$$

The brackets $\langle \rangle$ indicate an average with respect to the Gaussian action.

The perturbation theory can be formulated diagrammatically with solid and wavy lines indicating K^{-1} and D_0, respectively. Interactions in S_r are ring diagrams having hooks where wavy lines can attach, see Fig. 2. We then use a self-consistent procedure where a self-energy $\mathbf{\Sigma}_{\vec{q},\vec{q}'} \equiv \Sigma_{\vec{q}} \delta_{\vec{q},\vec{q}'}$ and a polarization $\mathbf{\Pi}_{\vec{q},\vec{q}'} \equiv \Pi_{\vec{q}} \delta_{\vec{q},\vec{q}'}$ are defined to renormalize $\mathbf{K}^{-1}$ and $\mathbf{D_0}$, respectively, according to the Dyson equations shown in Fig. 3.

The Dyson equations yield $\mathbf{K}_{\text{eff}} = \mathbf{K} - \mathbf{\Sigma}$ and $\mathbf{D}^{-1} = \mathbf{D_0^{-1}} - \mathbf{\Pi}$. The self-energy and the polarization are next approximated self-consistently by the diagrams in Fig. 4, which are equivalent to the equations

$$\Sigma_{\vec{q}} = -\sum_{\vec{p} \neq 0} K_{\text{eff} \, \vec{q}-\vec{p}}^{-1} D_{\vec{p}}, \tag{12}$$

$$\Pi_{\vec{q}} = -\frac{N_s}{2} \sum_{\vec{p}} K_{\text{eff} \, \vec{p}+\vec{q}}^{-1} K_{\text{eff} \, \vec{p}}^{-1} + \frac{N_s}{2} \sum_{\vec{p}} K_{\vec{p}+\vec{q}}^{-1} K_{\vec{p}}^{-1}. \tag{13}$$

Combining the Dyson equation for $\mathbf{D}^{-1}$ with Eqs. (8) and (13), the renormalized constraint propagator becomes

$$D_{\vec{q}}^{-1} = \frac{N_s}{2} \sum_{\vec{p}} K_{\text{eff} \, \vec{p}+\vec{q}}^{-1} K_{\text{eff} \, \vec{p}}^{-1}. \tag{14}$$
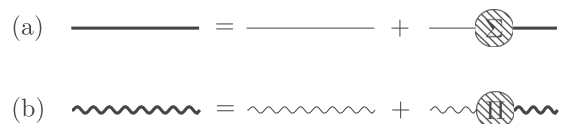

FIG. 3. Dyson equations for (a) the renormalized spin propagator K_{eff}^{-1} (bold solid line) and (b) the renormalized constraint propagator D (bold wavy line).
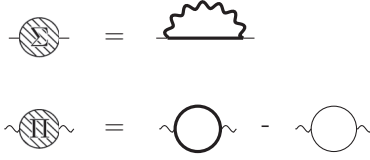
FIG. 4. Self-consistent equations for the self-energy and the polarization. The bold lines on the right hand sides also include the self-energy and the polarization.

The unrenormalized propagators can be expressed in terms of their renormalized equivalents so that $S[\Delta]$ becomes

$$S[\Delta] = -\beta V \Delta + \frac{N_s}{2} \mathrm{Tr} \ln \mathbf{K}_{\mathrm{eff}} + \frac{1}{2} \mathrm{Tr} \ln \mathbf{D}^{-1}$$
$$+ \frac{N_s}{2} \mathrm{Tr}(\mathbf{K}_{\mathrm{eff}}^{-1} \mathbf{\Sigma}) + S_R, \qquad (15)$$

where the remainder S_R is defined in Appendix A. In the following we will simply omit S_R, which means that after this omission $S[\Delta]$ includes all diagrams of the sort shown in Fig. 5, but neglects, among others, diagrams with vertex corrections shown in Fig. 6.

The final integral over Δ is performed using the saddle point approximation, see Appendix B, which gives the condition

$$\frac{N_s T}{2V} \sum_q K_{\mathrm{eff}}^{-1} \bar{q} = 1. \qquad (16)$$

By taking also into account the Gaussian fluctuations in Δ about the saddle point value and restoring omitted constants, we find the following expression for the free energy density $f = -\frac{1}{\beta V} \ln Z$:

$$f = -\Delta - \frac{N_s T}{2V} \sum_{\bar{q}} \ln \left(T K_{\mathrm{eff}}^{-1} \bar{q} \right) + \frac{N_s T}{2V} \sum_{\bar{q}} K_{\mathrm{eff}}^{-1} \bar{q} \Sigma_{\bar{q}}$$
$$+ \frac{T}{2V} \sum_{\bar{q}} \ln \left(T^2 D_{\bar{q}}^{-1}/2V \right) - \frac{(N_s - 1)T}{2} \ln \pi, \qquad (17)$$

where the $\ln D_{\bar{q}}^{-1}$–sum also includes the $\bar{q} = 0$ term. This expression is similar to that used in Ref. [18] in the context of the self-consistent screening approximation.

We solve the self-consistent equations (12) and (14) numerically, as described in details in Ref. [17], and obtain expressions for K_{eff}^{-1}, D, and Σ, which are then used to compute the free energy density from Eq. (17), and the static
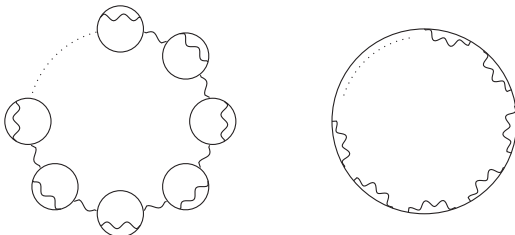

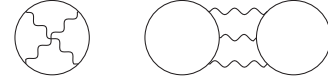FIG. 5. Diagrams included in the free energy.

FIG. 6. Leading order nonvanishing diagrams in S_R.

structure factor

$$\mathcal{S}(\vec{q}) \equiv \langle \vec{S}_{-\vec{q}} \cdot \vec{S}_{\vec{q}} \rangle = \frac{N_s T}{2} K_{\mathrm{eff}}^{-1} \bar{q}, \qquad (18)$$

as shown in Refs. [16,17]. We note that the saddle point condition Eq. (16) is equivalent to the condition $\langle \vec{S}_{\vec{r}} \cdot \vec{S}_{\vec{r}} \rangle = 1$.

III. J_1-J_2-J_3 MODEL

On the triangular lattice, the momentum space coupling function is

$$J_{\bar{q}} = J_1[\cos(q_1) + \cos(q_2) + \cos(q_3)]$$
$$+ J_2[\cos(q_1 - q_2) + \cos(q_2 - q_3) + \cos(q_3 - q_1)]$$
$$+ J_3[\cos(2q_1) + \cos(2q_2) + \cos(2q_3)], \qquad (19)$$

where $q_i \equiv \vec{q} \cdot \vec{a}_i$ and the lattice vectors are $\vec{a}_1 = \hat{x}$, $\vec{a}_2 = -\frac{1}{2}\hat{x} + \frac{\sqrt{3}}{2}\hat{y}$ and $\vec{a}_3 = -\frac{1}{2}\hat{x} - \frac{\sqrt{3}}{2}\hat{y}$. The lattice spacing has been set to unity. For further analysis, it is convenient to rewrite $J_{\bar{q}}$ as

$$J_{\bar{q}} = 2J_3 \left[\left(A_{\bar{q}} - \frac{1}{2} \left(1 - \frac{J_1}{2J_3} \right) \right)^2 \right] + (J_2 - 2J_3)B_{\bar{q}} + C, \qquad (20)$$

where $A_{\bar{q}} \equiv \cos(q_1) + \cos(q_2) + \cos(q_3)$, $B_{\bar{q}} \equiv \cos(q_1 - q_2) + \cos(q_2 - q_3) + \cos(q_3 - q_1)$, and C is a parameter-dependent constant. We will set $J_1 = -1$ (ferromagnetic) which defines our unit of energy.

By minimizing $J_{\bar{q}}$ with respect to $\vec{q}$, we can find which single-$\vec{q}$ states that minimize the energy. For generic choices of the parameters J_2 and J_3, these minimal $\vec{Q}$s form a discrete set of symmetry-related points in the Brillouin zone. The different regions of $\vec{Q}$s minimizing $J_{\bar{q}}$ are shown in Fig. 7, with the corresponding $\vec{Q}$s illustrated in Fig. 8. We define $\Gamma M(\Gamma K)$ as the lines connecting the Γ point and the M(K) points, illustrated by the green(blue) lines in Fig. 8. As shown in Ref. [9], the length of the $\vec{Q}$s minimizing $J_{\bar{q}}$ in region II is given by

$$Q_{\mathrm{II}} = \frac{2}{\sqrt{3}} \arccos \left(\frac{1 - J_2}{2J_2 + 4J_3} \right), \qquad (21)$$

while it in region III is given by

$$Q_{\mathrm{III}} = 2 \arccos \left(\frac{3J_2 - 2J_3 - \sqrt{(3J_2 + 2J_3)^2 + 8J_3}}{-8J_3} \right). \qquad (22)$$

On the border between regions II and III, where $J_2 = 2J_3$, the minimal $\vec{Q}$s form a continuous set defined by $A_{\bar{Q}} = \frac{1}{2}(1 - \frac{J_1}{J_2})$. This collection of minimal $\vec{Q}$s make a slightly deformed circular ring in momentum space. It is this border region which is of special interest in this paper.
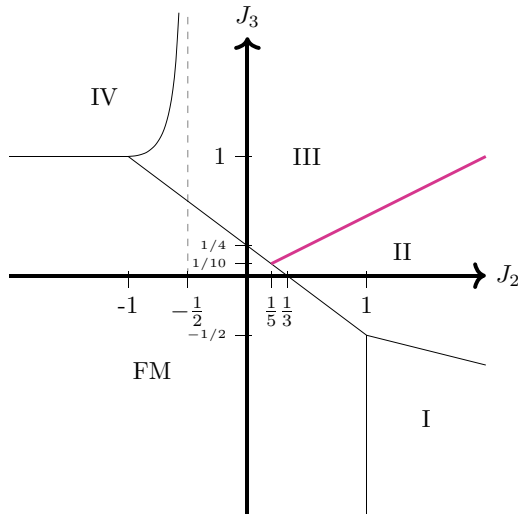
FIG. 7. Regions of different classes of wave vectors $\vec{Q}$ minimizing $J_{\vec{q}}$ for ferromagnetic nearest neighbor coupling, $J_1 = -1$. The pink thick line shows the II-III border, where the $\vec{Q}$s form a continuous set.

IV. RESULTS

A. Generic parameters

For generic parameter values, the $\vec{Q}$s form a discrete set, but it is only possible to break the point group symmetries of the lattice in regions I, II, and III. Such symmetry breaking is not possible in region IV, as all configurations are equivalent by a global spin rotation. In the regions I, II, and III, we in general find that the system exhibits a *single* first-order temperature-driven phase transition breaking rotational symmetry of the lattice. In Fig. 9 we show as an example of this the free energy density as a function of T for the point $(J_2, J_3) = (2, 0)$ in region II. From this figure, we see that there is a temperature region where the free energy density is
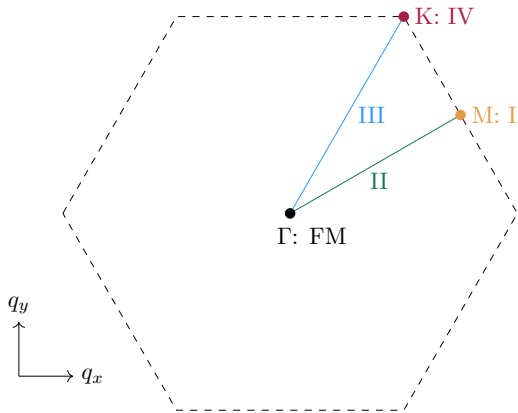

FIG. 8. Illustration of where the $\vec{Q}$s minimizing $J_{\vec{q}}$ are located in reciprocal space for the different regions from Fig. 7. The illustration is symmetric under rotations of $\frac{\pi}{3}$. The first Brillouin zone boundary is illustrated by the dashed lines. $\vec{Q}$ in the FM region is located at Γ (black point). In regions I and IV the $\vec{Q}$s are located at M (yellow points) and K (red points), respectively. Region II has $\vec{Q}$s along ΓM (green lines). In region III, the $\vec{Q}$s lie on ΓK (blue lines).
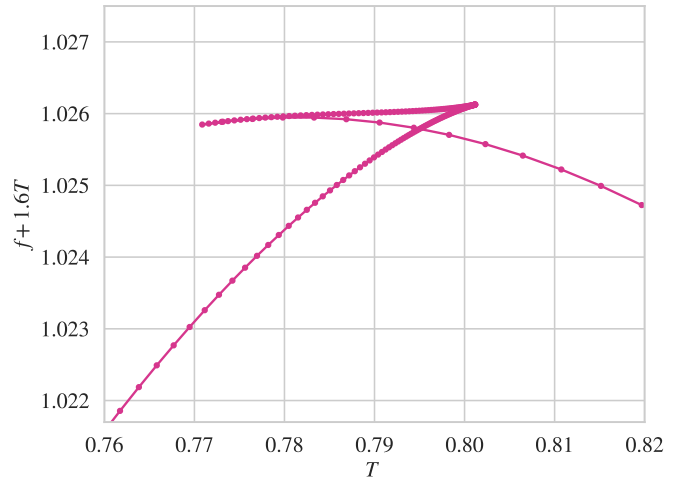

FIG. 9. Free energy density vs T for $(J_2, J_3) = (2, 0)$. $L = 200$. The free energy has been transformed by adding a linear term in T in order to better visualize the discontinuity in its derivative. The free energy density is multivalued in the region $T \in [0.770, 0.802]$.

multivalued. This multivaluedness reflects the fact that there are multiple values of Δ with associated self-energies Σ_q that lead to the same temperature when solving the saddle-point equation, Eq. (16). The thermodynamically stable states are those which minimize the free energy density. The existence of the corner point of the lowest free energy curve at $T_c = 0.795$ indicates a first-order phase transition there. Repeating this for other parameter points $(J_2, 0)$ and also for $(0, J_3)$, we find similar first-order phase transitions with critical temperatures given in Fig. 10.

Such a phase transition is between a high-T ring liquid phase where the static structure factor $\mathcal{S}(\vec{q})$ shows a ringlike feature in momentum space and a low-T phase where the system breaks the rotational symmetry of the lattice as it enters a single-$\vec{q}$ spiral state, where the pitch vector is determined by one of the minimal $\vec{Q}$s. Thus, in region I we generally get single-$\vec{q}$ states with $\vec{q} =$M and in region II(III) we generally get single-$\vec{q}$ states with $\vec{q}$ on ΓM(ΓK) with a length given
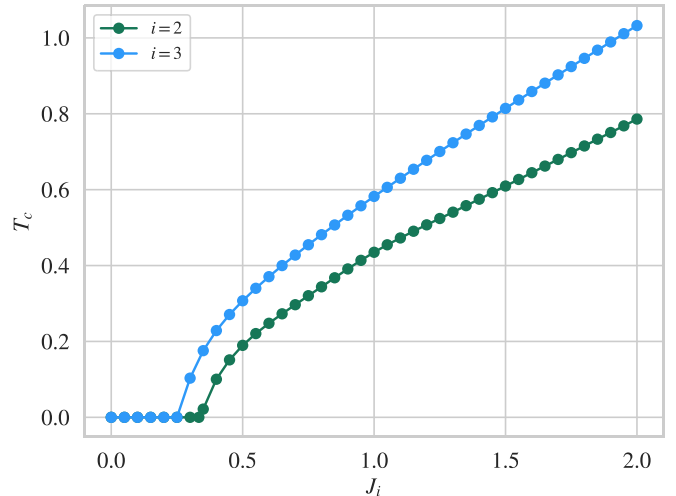

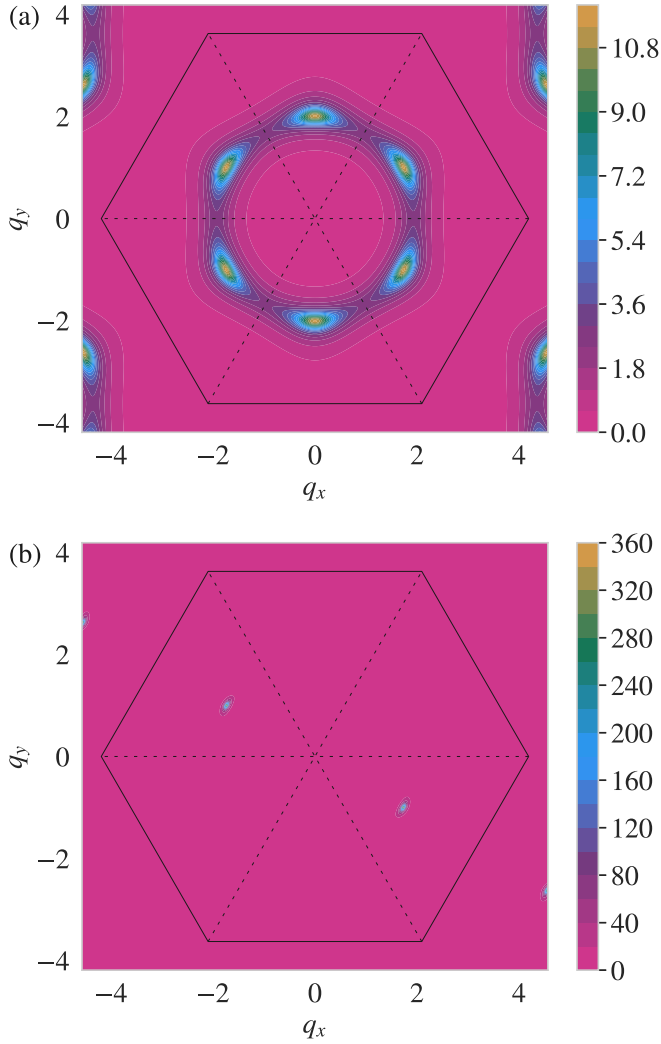FIG. 10. Critical temperatures along the J_2 and J_3 axis.

FIG. 11. Structure factors $\mathcal{S}(\vec{q})$ for a parameter point in region II, $(J_2, J_3) = (2, 0.5)$, for different temperatures: (a) high-T ring liquid phase at $T = 0.869$ and (b) low-T single-$\vec{q}$ phase with $\vec{q}$ on ΓM at $T = 0.868$. $L = 200$.
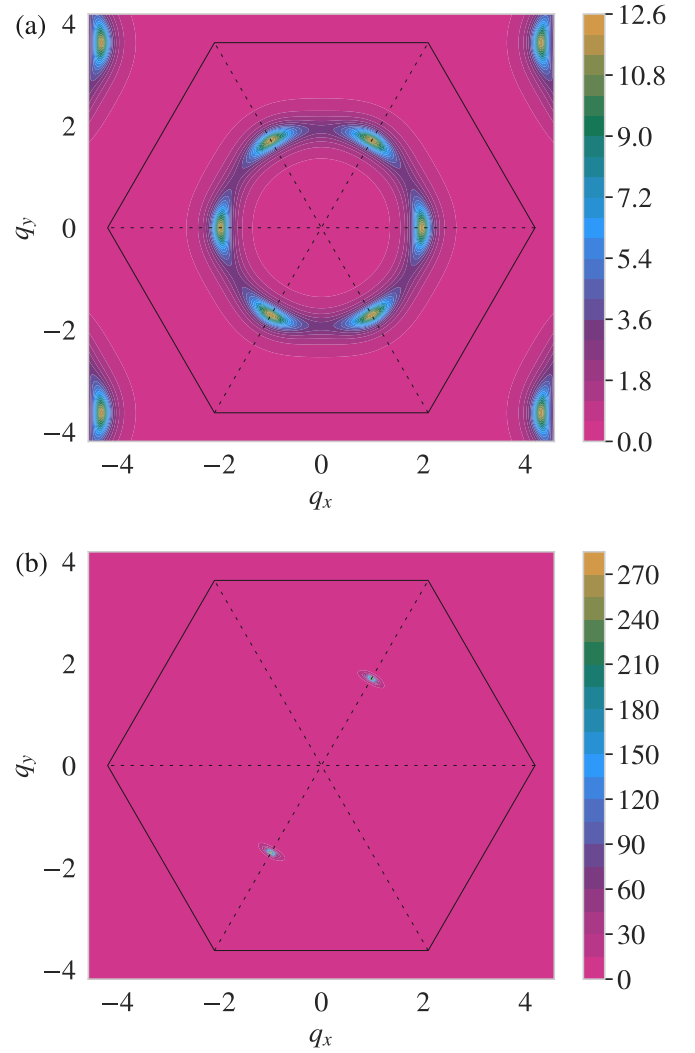

FIG. 12. Structure factors $\mathcal{S}(\vec{q})$ for a parameter point in region III, $(J_2, J_3) = (2, 1.5)$, for different temperatures: (a) high-T ring liquid phase at $T = 1.194$ and (b) low-T single-$\vec{q}$ phase with $\vec{q}$ on ΓK at $T = 1.191$. $L = 200$.

by Eqs. (21) and (22). Examples of both the high-T and low-T structure factors near the phase transition for a generic parameter point in region II(III) are shown in Fig. 11(Fig. 12).

The structure factor is inherently inversion symmetric, and a single-$\vec{q}$ state is thus characterized by *two* peaks in the structure factor (both $\vec{q}$ and $-\vec{q}$). If one however considers one of these peaks alone, it will keep mirror symmetry about one of the ΓM lines in regions I and II, while it in region III keeps mirror symmetry about one of the ΓK lines.

B. II-III border

For parameter values near the II-III border, on which the $\vec{Q}$s form a continuous set, the phase structure is more complicated. In particular we find that exactly on the border, $J_2 = 2J_3$, there are *two* consecutive phase transitions as the temperature is lowered. Figure 13 shows the structure factors in the three distinct phases. At high T the system is in the fully symmetric ring liquid phase where the structure factor shows

a ring, Fig. 13(a). Then below a first-order phase transition this ring is replaced by two partial rings/arcs, where only about one third of the full ring is present and centered on ΓM, Fig. 13(b). This arc structure factor breaks rotational symmetry, but is mirror symmetric about ΓM. We describe this regime in more detail in the following subsection. Then below this, there is a second phase transition into a single-$\vec{q}$ nonsymmetric phase where the structure factor has a narrow peak centered on a point $\vec{q}^*$ which is neither along ΓM nor ΓK, see Fig. 13(c). In fact, $\vec{q}^*$ rotates continuously towards the value predicted by the maximum entropy of spin waves around single-$\vec{q}$ spirals as the temperature is lowered, see Appendix C. This single-$\vec{q}$ phase breaks all the lattice symmetries except inversion symmetry. The free energy is qualitatively similar to Fig. 9 and shows a first-order phase transition between the ring liquid and the arc regime, but no apparent discontinuity in the derivative at the low-T phase transition. The breaking of the remaining lattice mirror symmetries of phase II should however be accompanied by a
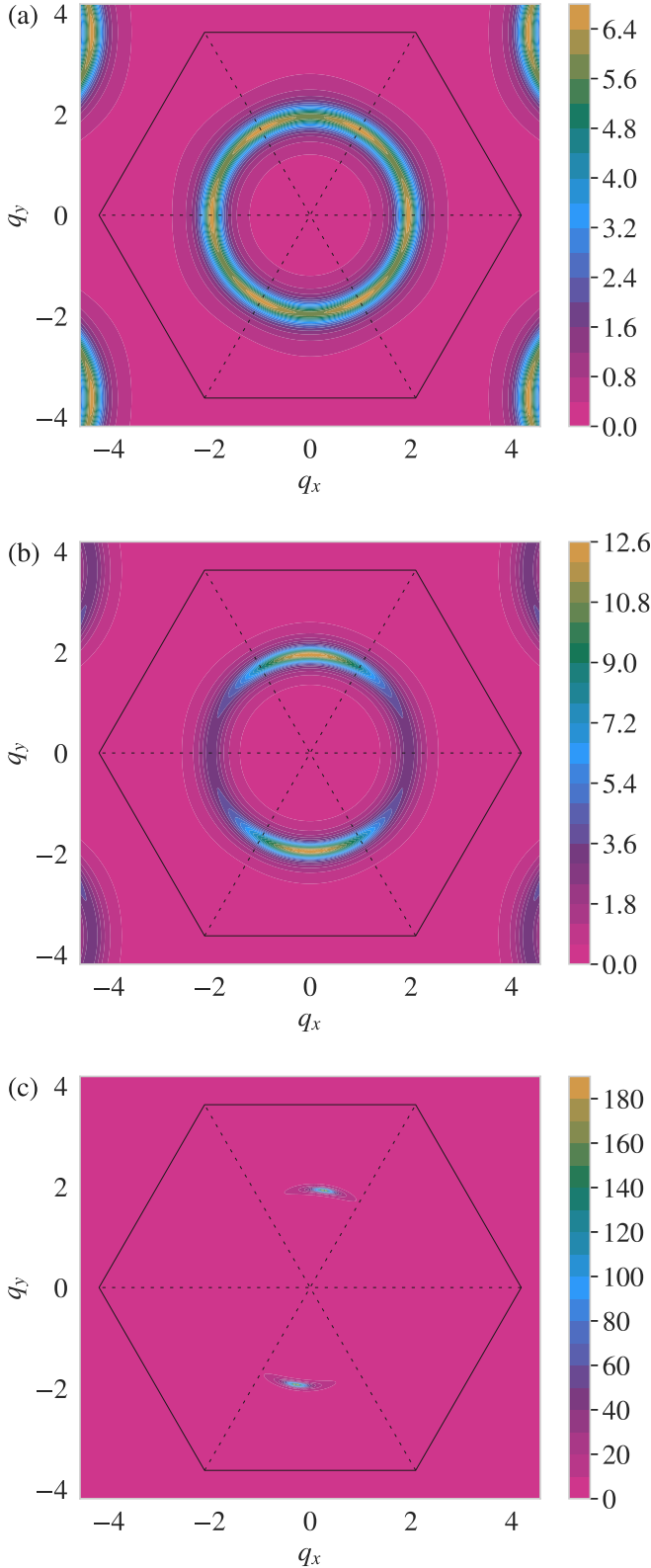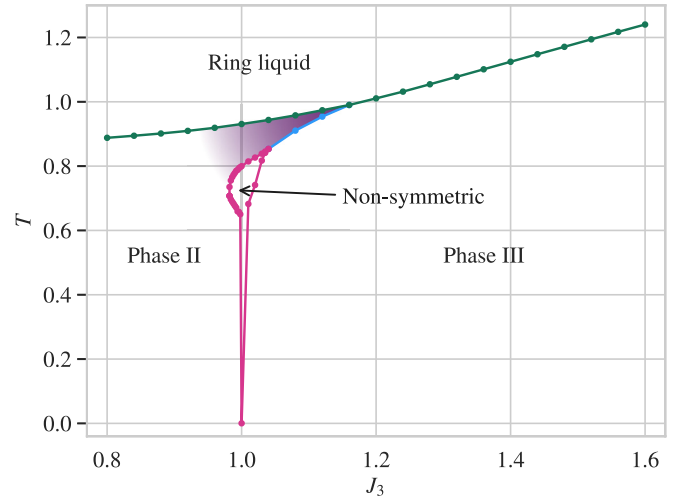
FIG. 14. Phase diagram for $J_2 = 2$. The purple region indicates the arc regime. The green and blue curves indicate first-order phase transitions, while the pink curve indicates continuous phase transitions. The II-III border is at $J_3 = 1$.

is continuous. The transition temperature is in this case found by considering the symmetries of the structure factor.

By investigating also J_3 values away from the II-III border for $J_2 = 2$ we establish the phase diagram shown in Fig. 14. The phase diagram shows four phases: At high T, we find the ring liquid phase, where all lattice symmetries are present. Phase II and phase III are in general single-$\vec{q}$ spiral states, where $\vec{q}$ is determined by the respective minima of $J_{\vec{q}}$. These phases break rotational symmetry while keeping some mirror symmetries. The nonsymmetric phase is a single-$\vec{q}$ spiral state in which both the rotational symmetry and all the mirror symmetries are broken. The arc regime, discussed below, is shown in purple. This regime is continuously connected to phase II, while a first-order phase transition separates it from phase III.

C. Arc regime

The structure factor arc, Fig. 13(b), has the same symmetries as the single-$\vec{q}$ phase in region II where the peak is centered on ΓM. However, the structure factor arc near the II-III border cannot be characterized as a single-$\vec{q}$ state as the arc length covers almost a quarter of the full circle. Figure 15 shows how the angular length of the arc and the position of its maximum change as the II-III border is approached from the region II side. The arc length increases monotonically, while the maximum intensity is on ΓM.

Intriguingly, we see from Fig. 14 that the arc regime (purple region) also extends into the region III side of the II-III border where $J_{\vec{q}}$ develops minima at ΓK. On this side, the arc intensity develops a split maximum with two peaks located symmetrically about ΓM. These peaks approach ΓK as J_3 is increased, as seen for $J_3 > 1$ in Fig. 15. Examples of the arc intensity just below the highest T_c for different J_3 are shown in Fig. 16. These intensity shapes depend also on the temperature: When lowering the temperature from T_c, the split peaks move towards ΓM. Figure 17 shows where the arc intensity has its maximum on ΓM and where the maximum is

FIG. 13. Structure factors $\mathcal{S}(\vec{q})$ at the II-III border, $(J_2, J_3) = (2, 1)$, for different temperatures: (a) high-T ring liquid phase at $T = 0.943$, (b) intermediate arc regime at $T = 0.927$, and (c) low-T nonsymmetric phase at $T = 0.788$. $L = 200$.

phase transition, and thus we conclude that the low-T phase transition between the arc regime and the nonsymmetric phase
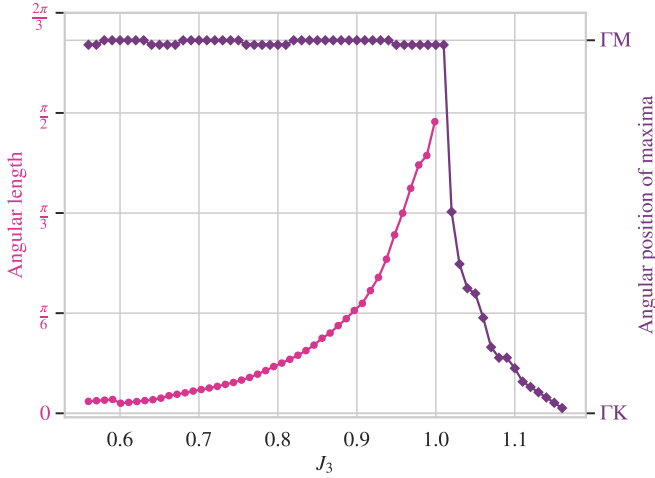
FIG. 15. Properties of the structure factor arc at the highest T_c for $J_2 = 2$. $L = 500$. Pink circles: Angular length of the structure factor arc defined as the full width at half maximum. Purple diamonds: The angular position of the maximum/maxima of the structure factor. The arc is always centered on ΓM, thus there is a split maximum for $J_3 > 1$.

split. The arc regime exists also for other values of J_2 near the II-III border, see Fig. 18.

V. DISCUSSION

The behavior of the J_1-J_2-J_3 Heisenberg model on the triangular lattice with $J_1 < 0$ is well understood for the whole parameter space at low temperatures: When the $\vec{Q}$s form a discrete set in regions I, II, and III, the system breaks lattice rotational symmetry by forming one of the single-$\vec{q}$ spiral states with minimal energy. Wherever the $\vec{Q}$s form a continuous set, i.e., at the II-III border, the degeneracy is lifted by the spin wave entropy, and the system breaks lattice rotational symmetry by forming one of the single-$\vec{q}$ spiral states with maximal entropy.
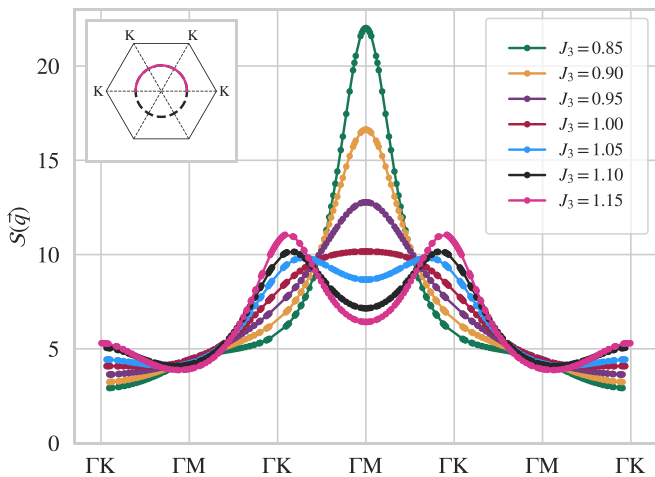

FIG. 16. The arc intensity at constant $|\vec{q}|$ for T just below the highest T_c and $J_2 = 2$. $L = 800$. The horizontal axis shows the angular variation of $\vec{q}$, illustrated by the pink solid line in the inset.
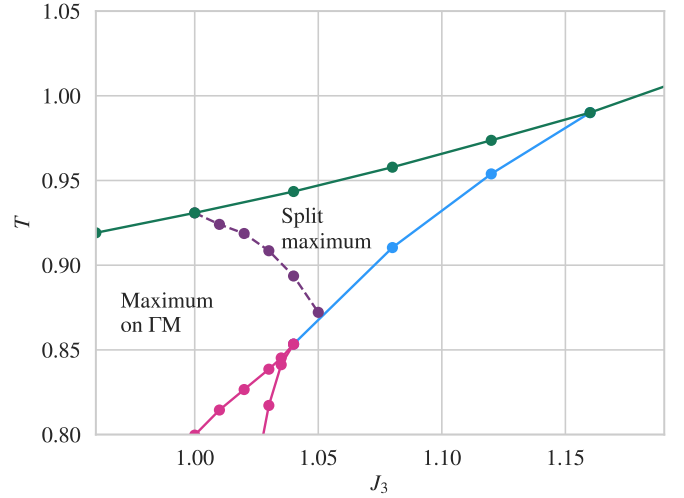

FIG. 17. Cutout of Fig. 14. The purple dashed line shows where the maximum of the arc intensity goes from being on ΓM to splitting into two maxima located symmetrically about ΓM. $J_2 = 2$.

In the discrete case, we find that the transition into the low-T ordered phase from the high-T symmetric state is generally a direct first-order phase transition. This is in agreement with Monte Carlo simulations on the triangular J_1-J_3 model [13,19]. The critical temperatures obtained in this paper are however likely to be overestimated as was seen in Ref. [17] for layered square lattices. We believe this is caused by the neglect of fluctuations associated with vertex corrections in the NBT. We have made sure that all of our results are carried out at a sufficiently large system size, so that increasing it only gives minor corrections.

Close to the II-III border the phase transition is not direct. Instead, as the temperature is lowered from the high-T phase, there is a first-order phase transition to an intermediate
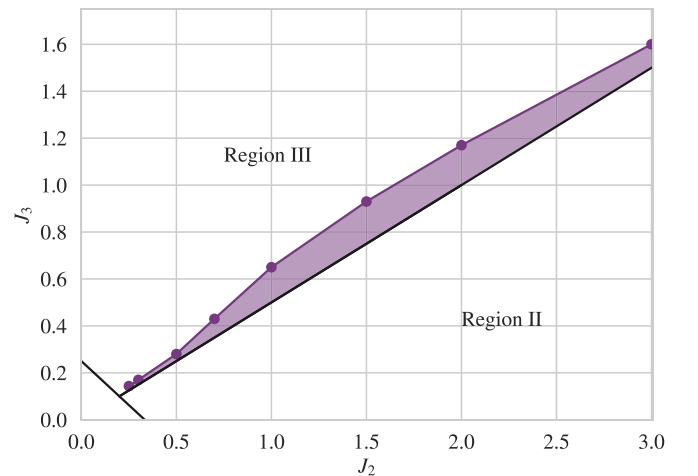

FIG. 18. An illustration of where in parameter space the arc regime exists. We have only studied $J_2 \leqslant 3$. The arc regime also exists on the region II side of the II-III border. However, as the arc regime is continuously connected to phase II, it cannot be distinguished from phase II in a well-defined way, as shown for $J_2 = 2$ in Fig. 14.

regime: the arc regime. Then at lower T there is a second transition. If the system is at or very close to the II-III border, this second transition is a continuous phase transition into the nonsymmetric single-$\vec{q}$ phase. In this phase, the pitch vector of the spiral changes continuously as T is further lowered and reaches eventually the value maximizing the spin wave entropy. Further into the region III side of the II-III border, the second phase transition becomes first-order into the single-$\vec{q}$ phase III. Such two-step pattern of symmetry breaking vaguely resembles the well-known hexatic melting scenario where the system with broken orientational and translational order is melted via an intermediate hexatic phase which breaks translational, but not orientational, order [20,21].

The structure factor arc has the same symmetries as the single-$\vec{q}$ states in phase II. Nevertheless the structure factor arc cannot be characterized as a single-$\vec{q}$ state. In fact, the static structure factor of the arc resembles rather the high-T ring liquid, but with portions of the ring removed. If one interprets the ring liquid as a spiral liquid consisting of a collection of short spirals with pitch vectors free to point in any direction, but constrained to have magnitudes lying on the manifold $\vec{Q}$, it is natural to conjecture that the arc is similar, but with the orientation of the spiral pitch vectors restricted to a distribution about one ΓM. This would also explain the split maximum of the arc intensity towards ΓK, as domains with single-$\vec{q}$ spirals along ΓK become energetically favorable on the region III side of the II-III border. However, the coexistence of many spirals is far from trivial and leads naturally to the consideration of energy and entropy of domain walls between single-$\vec{q}$ spiral domains. A very impressive characterization and observation of these has recently been done for helical magnets where the pitch vector is perpendicular to the spiral plane [22–24]. In particular bisector domain walls, where the domain wall bisects the two pitch vector orientations on either side, are favorable energetically. The analysis of how such domain walls lead to phase transitions must also include their entropy induced by kinks and spin waves. Such an analysis for the *Ising* model with extended range interactions on the triangular lattice showed that double domain walls [25] lead to an intermediate nematic phase [26]. We note that stable *point* defects can also exist in triangular lattice antiferromagnets [27], but their role in breaking lattice symmetries is unclear. In order to understand the arc regime, lattice details must also be accounted for to explain why the arc is centered on ΓM and not on ΓK.

The structure factor arc resembles strikingly the half moon patterns seen in simulations [28] and experiments [29] on kagome and pyrochlore lattices. These half moons occur both in the dynamic [30] and static structure factors [31], however they do not break lattice rotational symmetry. Furthermore, the static half moons are a consequence of having several atoms in the unit cell, as the half moon is the complement of the flat band combined with another dispersive band with a continuous minimum [31]. Thus, except for their appearance, it is not clear if or how the structure factor arc is related to the half moons.

It is pertinent to contrast the result obtained here to that obtained for the J_1-J_2-J_3 Heisenberg model on the square lattice. Among other results, Ref. [8] found an intermediate vortex crystal phase between the single-$\vec{q}$ and the ring liquid

at a single parameter point where the $\vec{Q}$s form a continuous set. The vortex crystal state has a structure factor peaked on four particular momentum vectors. Such a state is favorable when all these four momentum vectors lie at or very near the minimal $J_{\vec{q}}$ contour. We have attempted construction of similar combinations of 3-$\vec{q}$ and 4-$\vec{q}$ states for the triangular lattice J_1-J_2-J_3 model, but have not found a suitable candidate that keeps the spins normalized, and where all the $\vec{q}$'s minimize $J_{\vec{q}}$ simultaneously. In any case, if there is such a candidate, the resulting vortex crystal would probably only exist in a narrow range about one particular parameter point and not for such an extended region in parameter space as we have found the arc regime.

To strengthen the validity of our findings, it would be very valuable if our results could be confirmed by independent Monte Carlo simulations. We also hope that future research will properly explain the origin of the arc regime. Experimentally, the results obtained in this paper should be relevant for any magnetic material that can be described by the classical J_1-J_2-J_3 Heisenberg model on the triangular lattice with ferromagnetic J_1. In such materials, the first-order magnetic lattice symmetry breaking phase transitions, that we have found to occur over large portions of the phase diagram, may also be accompanied by concomitant structural instabilities triggered through magnetoelastic couplings [32]. An experimental observation of the arc regime will probably have to await a genuinely tunable magnet where the coupling parameters can be adjusted so that the minimal $\vec{Q}$s form a continuous set. We note that a magnetic system with tunable anisotropy has already been realized with cold atoms [33]. The NBT method used here can also be employed to investigate other spiral liquids, such as the extended Heisenberg model on the diamond lattice, relevant for the material $MnSc_2S_4$ [34].

APPENDIX A: S_R

In Eq. (15), $S[\Delta]$ is expressed in terms of renormalized propagators and a remainder

$$S_R \equiv -\frac{N_s}{2} \sum_{n=1}^{\infty} \frac{n-1}{n} \mathrm{Tr}(\mathbf{K}^{-1}\boldsymbol{\Sigma})^n + \frac{1}{2} \sum_{n=1}^{\infty} \frac{1}{n} \mathrm{Tr}(\mathbf{D}_0\boldsymbol{\Pi})^n$$
$$- \ln\langle e^{-S_r}\rangle, \tag{A1}$$

where it is understood in Eq. (15) that the $\vec{q} = 0$ contribution must be omitted when evaluating $\mathrm{Tr}\ln\mathbf{D}^{-1}$ and $\mathrm{Tr}(\mathbf{D}_0\boldsymbol{\Pi})^n$. In arriving at this expression we have added and subtracted a term

$$\frac{N_s}{2}\mathrm{Tr}(\mathbf{K}_{\mathrm{eff}}^{-1}\boldsymbol{\Sigma}) = \frac{N_s}{2} \sum_{n=1}^{\infty} \mathrm{Tr}(\mathbf{K}^{-1}\boldsymbol{\Sigma})^n \tag{A2}$$

so as to cancel the term $\mathrm{Tr}(\mathbf{K}^{-1}\boldsymbol{\Sigma})$ in S_R. This term causes S_R to be $\mathcal{O}(N_s^0)$ as there are no single-ring diagrams with one

wavy line in $\ln \langle e^{-S_r} \rangle$. The term $\ln \langle e^{-S_r} \rangle$ can be evaluated using the cumulant expansion and consists of all connected diagrams of rings with three or more wavy hooks. Each wavy line carries a factor D which is $\mathcal{O}(1/N_s)$ and each ring with n wavy hooks a factor $N_s(-i)^n/2n$ and n factors of K^{-1}. Momentum is conserved at every vertex.

Many diagrams cancel each other in S_R, in particular the types shown in Fig. 5. To see this, take first the connected diagram with $m \geqslant 1$ identical rings each with $2k$ hooks contracted sequentially in the fashion shown in Fig. 5 left for the case $k = 2$. The mth cumulant of $-\ln \langle e^{-S_r} \rangle$ gives this diagram with a combinatorial factor $-(-1)^{km}(1/2)^{sm}/2m$ where s is a symmetry factor which is 1 if the ring with $2k$ hooks is symmetric when flipped about its external wavy lines and zero otherwise. The term $\frac{1}{2m}\text{Tr}(\mathbf{D_0\Pi})^m$ gives also this diagram when $\mathbf{\Pi}$ is expanded to the $k-1$th order in the self-energy. In fact, it gives the same contribution but with opposite sign. In the cases when the external hooks on each ring are nearest neighbors, like the diagram Fig. 5 left, there are additional contributions. The first comes from the term $-\frac{N_s(k-1)}{2k}\text{Tr}(\mathbf{K}^{-1}\mathbf{\Sigma})^k$ where one of the $\mathbf{\Sigma}$ is written in terms of the full propagator $\mathbf{D}$ which in turn is expanded to the $m-1$th power in the polarization, while the rest are replaced with its lowest order contribution. This gives the combinatorial factor $-(-1)^k(k-1)/2$. The second contribution, which cancels the first, comes from the term $\frac{1}{2}\text{Tr}(\mathbf{D_0\Pi})$ when expanding the polarization in terms of the self-energy to the $k-1$th power and then replacing one of the self-energies with the full propagator D and the rest with D_0. Therefore all these diagrams vanish in S_R. Similarly the single ring diagram with k sequential wavy lines shown in Fig. 5 right will also vanish. Adding together the combinatorial factors: $-1/2k + 1/2 - (k-1)/2k$ that comes from the terms $-\ln \langle e^{-S_r} \rangle$, $\frac{1}{2}\text{Tr}(\mathbf{D_0\Pi})$ and $-\frac{N_s(k-1)}{2k}\text{Tr}(\mathbf{K}^{-1}\mathbf{\Sigma})^k$, respectively, we get zero.

APPENDIX B: SADDLE POINT

The saddle point method including Gaussian corrections gives

$$\int (-i)d\Delta e^{-S[\Delta]} \propto e^{-S[\Delta_0]-\frac{1}{2}\ln\left(-\frac{\partial^2 S[\Delta]}{\partial\Delta^2}\right)|_{\Delta=\Delta_0}}, \quad \text{(B1)}$$

where the saddle point value of Δ is determined by setting $\frac{\partial S}{\partial \Delta} = 0$. We have here restored the factor $-i$ which comes from changing the variable $\lambda_{\vec{q}=0} = -i\Delta$. Differentiating $S[\Delta]$ gives

$$\frac{\partial S[\Delta]}{\partial\Delta} = -\beta V + \frac{N_s}{2}\text{Tr}\left(\mathbf{K}_{\text{eff}}^{-1}\left(1 - \frac{\partial\mathbf{\Sigma}}{\partial\Delta}\right)\right) + \frac{1}{2}\text{Tr}\mathbf{D}\frac{\partial\mathbf{D}^{-1}}{\partial\Delta}$$
$$+ \frac{N_s}{2}\text{Tr}\left(\frac{\partial\mathbf{K}_{\text{eff}}^{-1}}{\partial\Delta}\mathbf{\Sigma} + \mathbf{K}_{\text{eff}}^{-1}\frac{\partial\mathbf{\Sigma}}{\partial\Delta}\right). \quad \text{(B2)}$$

This can be simplified by using Eq. (14) to deduce

$$\frac{\partial D_{\vec{q}}^{-1}}{\partial\Delta} = N_s \sum_{\vec{p}} K_{\text{eff}\ \vec{p}+\vec{q}}^{-1}\frac{\partial K_{\text{eff}\ \vec{q}}^{-1}}{\partial\Delta}, \quad \text{(B3)}$$

and Eq. (12) to rewrite the self-energy. It follows that

$$\frac{\partial S[\Delta]}{\partial\Delta} = -\beta V + \frac{N_s}{2}\text{Tr}\mathbf{K}_{\text{eff}}^{-1}, \quad \text{(B4)}$$
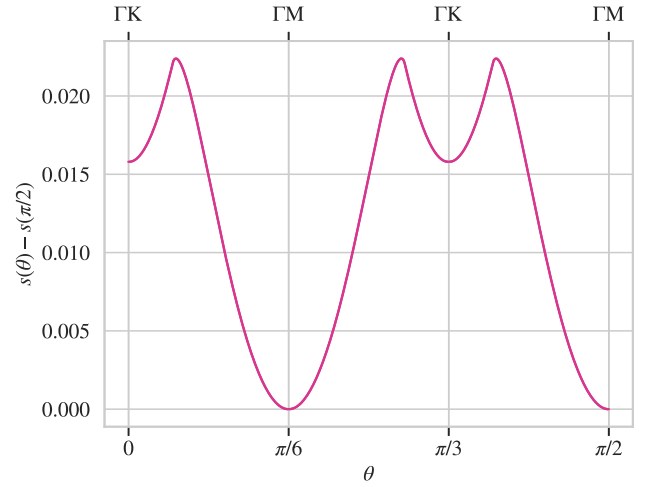

FIG. 19. Entropy of spin wave fluctuations around an ordered single-$\vec{q}$ spiral state for $(J_2, J_3) = (2, 1)$. The spiral pitch vector $\vec{q}$ lies along the ringlike minimum of $J_{\vec{q}}$ with an angle θ relative to the q_x axis.

which implies the saddle point condition Eq. (16).

The second derivative is

$$\frac{\partial^2 S[\Delta]}{\partial\Delta^2} = -\frac{N_s}{2}\text{Tr}\left(\mathbf{K}_{\text{eff}}^{-1}\mathbf{K}_{\text{eff}}^{-1}\left(1 - \frac{\partial\mathbf{\Sigma}}{\partial\Delta}\right)\right) \approx -D_{\vec{q}=0}^{-1}, \quad \text{(B5)}$$

where we have neglected $\frac{\partial\mathbf{\Sigma}}{\partial\Delta}$ as it is $\mathcal{O}(1/N_s)$. The Gaussian correction to the saddle point gives thus the missing $\vec{q} = 0$ part of the $\ln D_{\vec{q}}^{-1}$–sum in the free energy.

APPENDIX C: SPIN WAVE ENTROPY

The spin wave entropy per spin is given by

$$s = -\frac{1}{V}\sum_{\vec{k}}\ln\beta\omega_{\vec{k}}, \quad \text{(C1)}$$

where $\omega_{\vec{k}}$ is the spin wave dispersion. As shown in Ref. [8], the spin wave dispersion around an ordered planar single-$\vec{q}$
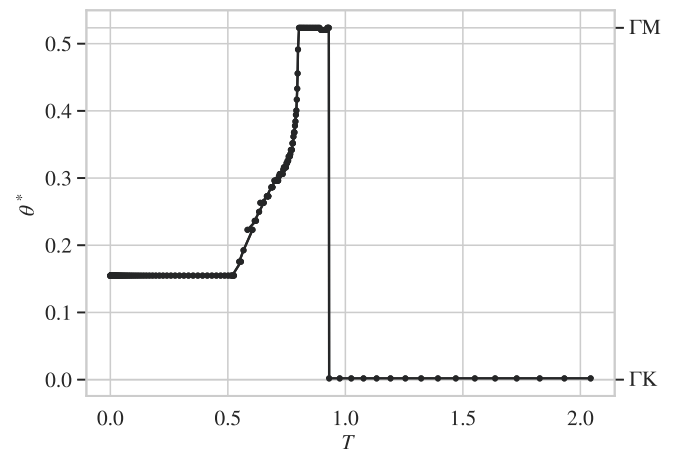

FIG. 20. Angular position of the maximum of $\mathcal{S}(\vec{q})$ as function of T on the II-III border, $(J_2, J_3) = (2, 1)$. $L = 1000$.

spiral state characterized by a pitch vector $\vec{Q}$ is

$$\omega_{\vec{k}} = \sqrt{\frac{1}{2}[J_{\vec{Q}+\vec{k}} + J_{\vec{Q}-\vec{k}} - 2J_{\vec{Q}}][J_{\vec{k}} - J_{\vec{Q}}]}. \quad \text{(C2)}$$

This result is strictly only valid where there is true long-range magnetic order at $T = 0$. We assume here that we can nevertheless use it to find the $\vec{Q}$s with maximum entropy also at low T where the spin correlation length is large. The spin wave entropy for the minimal $\vec{Q}$s when $(J_2, J_3) = (2, 1)$ is shown in

Fig. 19. We have taken the entropy to be zero at ΓM. Taking θ to be the angle between $\vec{Q}$ and the q_x axis, we find that the spin wave entropy has its maximum for $\theta = 0.154$ and symmetry-related values.

Figure 20 shows how the position $\vec{q}^*$ of the maximum of $\mathcal{S}(\vec{q})$ varies with temperature for $(J_2, J_3) = (2, 1)$. In the nonsymmetric phase ($T < 0.80$), the angular position θ^* of $\vec{q}^*$ changes continuously from $\theta^* = \pi/6$ (ΓM) to $\theta^* = 0.155$, which is very close to the value predicted by the spin wave entropy.

[1] N. D. Mermin and H. Wagner, Phys. Rev. Lett. **17**, 1133 (1966).

[2] J. Villain, J. Phys. (France) **38**, 385 (1977).

[3] J. Villain, R. Bidaux, J.-P. Carton, and R. Conte, J. Phys. (France) **41**, 1263 (1980).

[4] C. L. Henley, Phys. Rev. Lett. **62**, 2056 (1989).

[5] P. Chandra, P. Coleman, and A. I. Larkin, Phys. Rev. Lett. **64**, 88 (1990).

[6] A. Mulder, R. Ganesh, L. Capriotti, and A. Paramekanti, Phys. Rev. B **81**, 214419 (2010).

[7] S. Okumura, H. Kawamura, T. Okubo, and Y. Motome, J. Phys. Soc. Jpn. **79**, 114705 (2010).

[8] L. Seabra, P. Sindzingre, T. Momoi, and N. Shannon, Phys. Rev. B **93**, 085132 (2016).

[9] E. Rastelli, A. Tassi, and L. Reatto, Phys. B: Condens. Matter **97**, 1 (1979).

[10] T. Okubo, S. Chung, and H. Kawamura, Phys. Rev. Lett. **108**, 017206 (2012).

[11] S. Nakatsuji, Y. Nambu, K. Onuma, S. Jonas, C. Broholm, and Y. Maeno, J. Phys.: Condens. Matter **19**, 145232 (2007).

[12] I. I. Mazin, Phys. Rev. B **76**, 140406(R) (2007).

[13] R. Tamura and N. Kawashima, J. Phys. Soc. Jpn. **77**, 103002 (2008).

[14] J. Iaconis, C.-X. Liu, G. Halász, and L. Balents, SciPost Physics **4**, 003 (2018).

[15] S.-S. Gong, W. Zheng, M. Lee, Y.-M. Lu, and D. N. Sheng, Phys. Rev. B **100**, 241111(R) (2019).

[16] M. Schecter, O. F. Syljuåsen, and J. Paaske, Phys. Rev. Lett. **119**, 157202 (2017).

[17] O. F. Syljuåsen, J. Paaske, and M. Schecter, Phys. Rev. B **99**, 174404 (2019).

[18] D. G. Barci, A. Mendoza-Coto, and D. A. Stariolo, Phys. Rev. E **88**, 062140 (2013).

[19] R. Tamura and N. Kawashima, J. Phys. Soc. Jpn. **80**, 074008 (2011).

[20] B. I. Halperin and D. R. Nelson, Phys. Rev. Lett. **41**, 121 (1978).

[21] D. R. Nelson and B. I. Halperin, Phys. Rev. B **19**, 2457 (1979).

[22] F. Li, T. Nattermann, and V. L. Pokrovsky, Phys. Rev. Lett. **108**, 107203 (2012).

[23] P. Schoenherr, J. Müller, L. Köhler, A. Rosch, N. Kanazawa, Y. Tokura, M. Garst, and D. Meier, Nat. Phys. **14**, 465 (2018).

[24] T. Nattermann and V. L. Pokrovsky, J. Exp. Theor. Phys. **127**, 922 (2018).

[25] S. E. Korshunov, Phys. Rev. B **72**, 144417 (2005).

[26] A. Smerald, S. Korshunov, and F. Mila, Phys. Rev. Lett. **116**, 197201 (2016).

[27] H. Kawamura and S. Miyashita, J. Phys. Soc. Jpn. **53**, 4138 (1984).

[28] J. Robert, B. Canals, V. Simonet, and R. Ballou, Phys. Rev. Lett. **101**, 117207 (2008).

[29] S. Guitteny, J. Robert, P. Bonville, J. Ollivier, C. Decorse, P. Steffens, M. Boehm, H. Mutka, I. Mirebeau, and S. Petit, Phys. Rev. Lett. **111**, 087201 (2013).

[30] H. Yan, R. Pohle, and N. Shannon, Phys. Rev. B **98**, 140402(R) (2018).

[31] T. Mizoguchi, L. D. C. Jaubert, R. Moessner, and M. Udagawa, Phys. Rev. B **98**, 144446 (2018).

[32] C. Fang, H. Yao, W.-F. Tsai, J. P. Hu, and S. A. Kivelson, Phys. Rev. B **77**, 224509 (2008).

[33] P. N. Jepsen, J. Amato-Grill, I. Dimitrova, W. W. Ho, E. Demler, and W. Ketterle, Nature (London) **588**, 403 (2020).

[34] D. Bergman, J. Alicea, E. Gull, S. Trebst, and L. Balents, Nat. Phys. **3**, 487 (2007).